Dynamic characterization of sandwich beams using a LASER Vibrometer

Simão Pedro Lima Carvalho
simao.carvalho@tecnico.ulisboa.pt s312415@studenti.polito.it

Instituto Superior Técnico, Politecnico di Torino

December 2023

Abstract

A **Modal Test** was conducted on four composite beams from the Laboratory of the Department of Mechanical and Aerospace Engineering at Politecnico di Torino, under **Free-free condition**. These beams featured 7075 aluminium faces and a WF-110 polymer foam core, with varying material thicknesses across the beams. Furthermore, **Finite Element Models** were created for each structure, and numerical analyses were performed on these models. It's noteworthy that in this work, unlike the usual modal test practice, a **Laser Doppler Vibrometer** was used for response measurement, as part of an effort to explore the viability of this technology for **modal testing**. After analyzing the resonant frequencies and vibration modes of the structures, the results from both models were compared. This comparison confirmed the accuracy of the previously developed **FEM** models. It also underscored the good performance of the structure designed for simulating **Free-free condition** tests and highlighted the significant potential of **LDVs** for **modal testing**.
Keywords: FEM, Free-free condition, Modal Testing, LDV

1. Introduction

Throughout generations, humanity has witnessed significant technological advancements driven by the need to fulfill various requirements. However, as technological demands increased, especially in the aerospace and automotive industries, conventional materials began to demonstrate limitations in terms of performance. To address these needs, researchers recognized that by combining different materials, they could create a final product with optimized properties [1]. Therefore, extensive research has been conducted in the field of composite materials [2].

Consequently, for this work, four composite beams from the Laboratory of the Department of Mechanical and Aerospace Engineering at Politecnico di Torino were dynamically studied through modal tests. These beams all featured 7075 aluminium faces and a core of WF-110 polymer foam. However, variations in material thickness from one beam to another led to differences in stiffness and distributed mass among the beams. As a result, these stiffness variations translated into distinct dynamic characteristics when external forces were applied using a Shaker.

1.1. Topic Overview

The primary goal of this work is to conduct modal testing on four composite beams, making modal testing the central focus of this work.

Modal testing, in essence, encompasses a set of experimental techniques designed to explore the behaviour of systems under dynamic loads. Through these experimental methods, it becomes feasible to determine specific modal characteristics of each structure, such as natural frequencies, modal shapes, and damping. Understanding these characteristics subsequently allows for predictions regarding the structural response under dynamic loads [3, 4].

It's important to note that prior to conducting any modal test, it's customary to create an initial Finite Element Model (FEM) that accurately represents the structure under investigation [5]. Following the modal test execution, the quality of these numerical models should be assessed by comparing them to the experimentally obtained results.

With that in mind, engineers commonly use accelerometers to measure a structure's response [6, 7, 8], but this method has potential errors. Accelerometers introduce additional mass to the structure, which can significantly alter the characteristics of lightweight structures [9]. To enhance precision and reliability, an alternative method employs Laser Doppler Vibrometry (LDV) for data acquisition.

1.2. Objectives and Deliverables

One of the main objectives of this work is to conduct modal testing on four beams in a Free-free condition state. However, as suspending a beam in the air without any support is infeasible, an approximation to the Free-free condition scenario was devised.

Another objective is to create accurate FEM models for each of the four beams, predicting their dynamic behavior. After obtaining results from both numerical and experimental models, the work aims to develop programs for data collection and analysis, assessing the correlation between the models to validate the constructed FEM models.

In addition, this work aims to define an optimal point configuration for the LDV to accurately represent modal shapes. Furthermore, it seeks to evaluate the potential of this technology for modal testing. For this reason, the potential advantages and disadvantages of LDV technology for these activities will also be discussed.

2. Dynamics of discrete systems

2.1. SDOF systems

Applying the Lagrange Equation to single-degree-of-freedom (SDOF) systems, which are systems that can be fully described using a single coordinate, yields Equation 2.1. It's important to note that in this equation, u represents displacement, $\dot{u}$ represents velocity, $\ddot{u}$ represents acceleration, k stands for stiffness, c for damping, m for mass, and F denotes the applied external force.

$$m\ddot{u} + c\dot{u} + ku = F \Leftrightarrow \ddot{u} + \frac{c}{m}\dot{u} + \frac{k}{m}u = \frac{F}{m} \quad (2.1)$$

Now, while various scenarios can be analyzed using Equation 2.1, the most relevant case to address is the situation of "Force vibrations for damped systems" meaning $F \neq 0$ and $c \neq 0$. In this case, the solution to Equation 2.1 can be expressed as $u(t) = u_f(t) + u_p(t)$, where $u_f(t)$ represents the homogeneous solution, and $u_p(t)$ is the particular solution of this differential equation. Therefore, the equation related to the particular solution can be written as follows:

$$\ddot{u_p} + \frac{c}{m}\dot{u_p} + \frac{k}{m}u_p = \frac{F}{m} \quad (2.2)$$

To describe $u_p(t)$ properly, it is essential to define $F(t)$ since the response is closely associated with the force acting on any system. Assuming that $F(t)$ behaves as a periodic function, it can be expressed as a linear combination of harmonic functions, such as $F(t) = F_0 e^{j\omega t}$. Therefore, when $F(t)$ is described by a harmonic function, the response should also be represented as a linear combination of harmonic functions. Its angular frequency will necessarily be the same as that of the force, but with a phase delay φ, as seen in $u_p(t) = u_0 e^{j\omega t + \varphi}$.

Therefore, by working with Equation 2.2 and recognizing that β corresponds to the **Frequency Ratio** (i.e., the ratio between the angular frequency of the external force and the natural angular frequency of the system under study, $\beta = \frac{\omega}{\omega_n}$), Equation 2.3 can be deduced as follows:

$$u_0 e^{-j\varphi} = \frac{F_0}{k} \cdot \frac{(-\beta^2) - j2\zeta\beta}{(1-\beta^2)^2 + 4\zeta^2\beta^2} \quad (2.3)$$

Additionally, it's easy to see that Equation 2.2 can now be written as follows:

$$-\omega^2 m u_0 e^{j(\omega t - \varphi)} + cj\omega u_0 e^{j(\omega t - \varphi)} + k u_0 e^{j(\omega t - \varphi)} = F_0 e^{j\omega t} \quad (2.4)$$

With that said, it's crucial to introduce the concept of the **Dynamic Amplification Factor**, denoted as $D(t)$. This factor allows us to assess how much the dynamic response is amplified compared to the static response, $u_{st}(t)$. Therefore, it is as follows:

$$D(t) = \frac{u_p(t)}{u_{st}(t)} = \frac{e^{j(\omega t - \varphi)}}{\sqrt{(1-\beta^2)^2 - 4\zeta^2\beta^2}} \quad (2.5)$$

To determine the maximum value of $D(t)$, it is only necessary to identify when $u_p(t)$ reaches its maximum. Therefore, D_{max} can be algebraically expressed as:

$$D_{max} = \frac{1}{\sqrt{(1-\beta^2)^2 - 4\zeta^2\beta^2}} \quad (2.6)$$

It's important to note that for $\zeta \geq \frac{\sqrt{2}}{2}$, the function D_{max} does not exhibit an absolute maximum value. However, for values of $\zeta < \frac{\sqrt{2}}{2}$, the function D_{max} consistently reaches an absolute maximum at $\beta = \sqrt{1-2\zeta^2}$, which is very close to $\beta = 1$. As ζ increases, the value of β at which the peak in D_{max} occurs decreases. When β is very close to 1, the angle φ approaches 90°, and in this case, the response is dominated by the damping force ($c\omega u_0$). This condition is known as **Resonance**, and as you will observe, it will be the primary focus of this work. A graphical representation of this scenario can be seen in Figure 2.1.

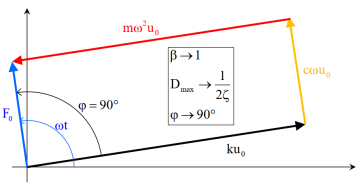

Figure 2.1: Geometric representation of Equation 2.4 as $\beta \to 1$ [5].

2.2. Frequency response

In many cases, analyzing the response in the time domain proves to be a very complex task, often

involving substantial computational costs or even being impossible to perform. To address this challenge, a common approach is to transform the time-domain response into the frequency domain. This conversion between domains is typically achieved using the **Fourier Transform** (FT):

$$F(\omega) = T\left[f(t)\right] = \frac{1}{\sqrt{2\pi}} \int_{-\infty}^{+\infty} f(t) e^{-j\omega} dt \quad (2.7)$$

Applying the Fourier transform to Equation 2.1, where $T(u) = U(\omega)$ and $T[F] = F(\omega)$, allow us to obtain the following result:

$$U(\omega) = \frac{1}{k \cdot \left[(1-\beta^2) + (j2\zeta\beta)\right]} \cdot F\left(\omega\right) \quad (2.8)$$

Equation 2.8 can be simplified by expressing $U(\omega)$ as $H(\omega) \cdot F(\omega)$, where $H(\omega)$ is referred to as the transfer function. This function can also be further simplified through the following expression: $H(\omega) = Me^{-j\varphi}$. Therefore, the amplitude M of $H(\omega)$ is determined by the following equation:

$$M = \frac{1}{k} \cdot \frac{1}{k\sqrt{\left(1-\beta^2\right)^2 + 4\zeta^2\beta^2}} = \frac{1}{k} \cdot D_{max} \quad (2.9)$$

Consequently, from Equation 2.9, it is clear that the amplitude of $H(\omega)$ is directly proportional to D_{max}. This relationship demonstrates that the frequency peaks of $H(\omega)$ coincide with the instances when the function D_{max} reaches its maximum value. In other words, the peaks of $H(\omega)$ occur under resonance conditions (when there is damping for $\beta \approx 1 \Rightarrow \omega_n \approx \omega$).

2.3. MDOF systems

Similar to SDOF systems, the equations of motion for this case are derived using Lagrange's equation. However, as it involves M degrees of freedom, the resulting equation is in matrix form:

$$[M]\{\ddot{u}\} + [C]\{\dot{u}\} + [K]\{u\} = \{F\} \quad (2.10)$$

In this case, it's useful to consider the following scenarios: free vibrations for undamped ($F = 0$ and $c = 0$), force vibrations for undamped ($F \neq 0$ and $c = 0$), and force vibrations for damped ($F \neq 0$ and $c \neq 0$).

- **Free vibrations for undamped systems**

  In this case, the equation 2.10 can be simplified as follows: $[M]\{\ddot{u}\} + [K]\{u\} = \{0\}$. Assuming that the response can be represented as $\{u\} = \{\phi\} e^{j\omega_n t}$, the result is:

  $$\left([k] - \omega_n^2 [M]\right)\{\phi\} e^{j\omega t} = \{0\} \quad (2.11)$$

  Upon analyzing Equation 2.11, it becomes evident that it can only be solved in two ways, however, the solution $\{\phi\} = 0$ is a trivial solution. Since the term related to the exponential will never be zero, this problem becomes an eigenvalue problem. That is:

  $$det\left([K] - \omega_n^2 [M]\right) = 0 \quad (2.12)$$

  Once the values of ω_n (eigenvalues) are obtained, they are substituted back into Equation 2.11 to obtain the eigenvectors, represented as $\{\phi\}$ corresponding to each ω_n value. Thus, through this substitution, a known vector $\left\{\hat{\phi}\right\}$ is obtained (modal vector), which is then multiplied by an unknown constant A_i $\left(\{\phi\}_i = A_i \cdot \left\{\hat{\phi}\right\}_i\right)$.

  With all the vectors $\{\phi\}_i$, it is possible to construct a modal matrix $[\phi]$, which is an $M \times M$ square matrix. This modal matrix proves to be highly useful because it enables the diagonalization of the stiffness and mass matrices ($[K]$ and $[M]$, respectively), significantly simplifying the calculations. It is achieved as follows: $[\phi]^T [K] [\phi] = [D_K]$ e $[\phi]^T [M] [\phi] = [D_M]$.

  Finally, it is also observed that for MDOF systems, the following expression is valid:

  $$\omega_{n_i}^2 = \frac{\{\phi\}_i^T [K] \{\phi\}_i}{\{\phi\}_i^T [M] \{\phi\}_i} \quad (2.13)$$

  However, it is not very practical because to apply it, one needs to determine the vectors (ϕ), which, as shown earlier, requires prior knowledge of the eigenvalues ω_{n_i}.

- **Force vibrations for undamped systems**

  In this case, Equation 2.10 can be simplified as follows: $[M]\{\ddot{u}\} + [K]\{u\} = \{F(t)\}$. It's evident that if the matrices $[M]$ and $[K]$ are not diagonal, solving this system can involve significant computational costs. Therefore, a common approach is to transform the physical coordinates into modal coordinates to diagonalize these matrices, as mentioned earlier. This transformation is applied as follows: $\{u(t)\} = [\phi] \cdot \{\nu(t)\}$

  Working in modal coordinates simplifies the problem as it allows the diagonalization of the system and the solution of M individual equations, similar to solving M-SDOFs systems This leads to the application of the TF, as previously done for SDOF systems. Thus, the expression $U(\omega) = [H(\omega)] F(\omega)$ is derived, where $H(\omega)$ is represented by the following expression:

  $$[H(\omega)] = \frac{[\phi] [\phi]^T}{\left([D_K] - \omega^2 [D_M]\right)} \quad (2.14)$$

  Typically, Equation 2.14 is represented as follows:

  $$H_{\alpha\eta}(\omega) = \sum_{k=1}^{N} \frac{\hat{\phi}_{k\alpha}\hat{\phi}_{k\eta}}{M_k\left(\omega_{n_k}^2 - \omega^2\right)} \quad (2.15)$$

It's important to note that the symbol α refers to the location where the response is measured, while the symbol η indicates the point where the structure is excited.

- **Force vibrations for damped systems**

  This case is described by Equation 2.10 and has not been considered until now because the matrix $[C]$ in Equation 2.10, unlike the matrices $[M]$ and $[K]$, is often not diagonalizable when multiplied by the modal shape matrices. Therefore, to address this matrix, it's necessary to experimentally determine the response and excitation in the frequency domain. This enables the acquisition of experimental values of $H(\omega)$ (see Equation 2.15). Subsequently, the theoretical expression of $H(\omega)$ is compared to these experimental values using appropriate software.

  However, Equation 2.15 does not include the damping term because it was derived for the situation of force vibrations in undamped systems. To obtain the expression for $H(\omega)$ that accounts for damping, an analogy with the situation of force vibrations for damped SDOF systems (see Equation 2.8) must be made. This analogy leads to the following expression:

$$H_{\alpha\eta}(\omega) = \sum_{k=1}^{N} \frac{\hat{\phi}_{k\alpha}\hat{\phi}_{k\eta}}{M_k\left(\omega_{n_k}^2 - \omega^2 + j2\zeta_k\omega_{n_k}\omega\right)} \quad (2.16)$$

3. Construction and Analysis of Numerical Models

In this study, the four beams, introduced in Chapter 1, are composite structures. They comprise *AL 7075* aluminium faces and a *WF 110* polymer foam core. These materials are isotropic, meaning their mechanical properties, such as Young's modulus (E), shear modulus (G), and Poisson's ratio (ν), remain consistent in all directions.

To define these materials, it's necessary to provide values for two out of the three unknowns: E, G, and ν. Additionally, the mass density (ρ) for each material must be specified for modal analyses. Table 3.1 shows these material properties. The geometric dimensions for both materials used in the beams are listed in Table 3.2

Property	**AL 7075**	**WF 110**
E [MPa]	67545.6	194.1
G [MPa]	25393.1	66.9
ν	0.33	0.45
ρ [Kg/m^3]	2750.6	109.5

Table 3.1: Values of the physical constants of the materials that make up the beams under study.

	Beam 1	**Beam 2**	**Beam 3**	**Beam 4**
Length [mm]	5000 ±0.5	5000 ±0.5	5000 ±0.5	5000 ±0.5
Width [mm]	800 ±0.5	800 ±0.5	800 ±0.5	800 ±0.5
Thick. [mm]	43.32 ±0.01	41.18 ±0.01	33.53 ±0.01	31.54 ±0.01
Thick. of faces [mm]	2	1	2	1
Thick. of core [mm]	39.32 ±0.01	39.18 ±0.01	29.53 ±0.01	29.54 ±0.01

Table 3.2: Results obtained for the modal forms of beam D02

With that said, the meshes for all beams were uniformly created. Solid elements (**Hexa8**) were used for the core, and Shell elements (**Quad4**) were used for the aluminium faces. In terms of subdivisions, the same configuration was applied to all the beams under study, meaning the length was divided into 250 finite elements (FE), the width into 20 FE, and the thickness into 10 FE. Finally, it is important to note that Finite Element Analysis (FEA) were conducted using the SOL 103 option in Patran.

3.1. FEA Results

It's worth noting that the structures under investigation, being simple rectangular beams, have resonance frequencies associated with specific modal shapes. These modes, which are consistent across all beams due to their identical dimensions, encompass flexural modes along the x-axis, torsional modes about the x-axis, and flexural modes along the y-axis.

For clarity in assessing resonance frequencies using LDV, only experimental measurements up to the 5^{th} flexural modal shape were considered for all beams. This decision was influenced by the complexity of this modal shape, characterized by 6 transverse nodal lines. The numerical results for each beam are summarized in Tables 6.1,6.2,6.3,6.4.

4. Experimental modal analysis

4.1. Modal testing

To conduct modal tests, various pieces of equipment are necessary, including one to measure the structures' responses to imposed excitations and another to apply the excitation. As previously mentioned, a Laser Doppler Vibrometer (LDV) was used for response measurements. This choice was made because common equipment (piezoelectric accelerometers) can introduce notable experimental errors. These errors are primarily because, despite being relatively small, the mass of these devices is not negligible, resulting in an effect known as **mass loading** [9].

An analysis of the coherence function (γ^2) was conducted to evaluate the quality of the data produced by LDV. This function compares the input signal through multiplication by its complex conjugate, aiming for an ideal coherence value of 1. In the presence of noise, γ^2 takes a positive but sub-unity value, indicating a decrease in coherence. This parameter assesses result quality by identifying noise that may affect the outcomes. The evaluation is described by Equation 4.1, with functions $G_{FF}(\omega)$ and $G_{FU}(\omega)$ denoting the **Average Auto-Spectrum of F** and the **Averaged Cross Spectrum between input F and output U**, respectively.

$$\gamma^2 = \frac{|G_{\mathrm{XY}}(\omega)|^2}{G_{\mathrm{XX}}(\omega)G_{\mathrm{YY}}(\omega)} \tag{4.1}$$

The choice of equipment to excite the systems considered two options: an **Impact Hammer** or a **Shaker**. The Shaker was selected for this study due to several advantages. With the Shaker, force excitation is applied by a machine, and although any machine or instrument always has some associated uncertainty, the amplitude of all vibrations is quite precise when using such devices. This reduces the risk of damaging the structures compared to using a Hammer. However, during the experiments, there were concerns that the Shaker's connection might introduce significant stiffness into the systems, potentially affecting the results. As a result, a complementary study was conducted using a Hammer to address this concern.

To evaluate the similarity between modal shapes obtained from a modal test and those generated by a numerical model, specific metric correlations are commonly used. One prominent correlation in this work is the Modal Assurance Coefficient (MAC), expressed numerically in Equation 4.2. Here, indices A and B represent the models under study for comparison, ϕ_r^A is modal shape r from model A, and ϕ_s^B is modal shape s from model B. The MAC's values range from 0 to 1. When it approaches 1, it indicates a high similarity between the compared modal shapes, while values closer to zero suggest significant differences between them.

$$MAC_{rs}^{AB} = \frac{\left|\{\phi_r^A\}\{\phi_s^B\}\right|^2}{\left(\{\phi_r^A\}^T \cdot \{\phi_r^A\}\right)\left(\{\phi_s^B\}^T \cdot \{\phi_s^B\}\right)} \tag{4.2}$$

4.2. Introduction of Polytec LDV

The Polytec Laser Doppler Vibrometer (LDV) is a device used to measure vibrations by employing laser light and is based on the Doppler effect. A representative illustration of this device is shown in Figure 4.1.

However, the LDV, while alleviating issues like Mass Loading, has its limitations. Notably, uncertainties exist regarding the laser radiation source's emissions, although these are generally minor and addressed by the LDV manufacturer.

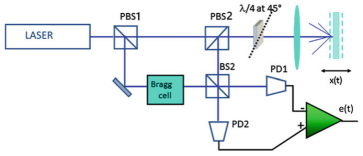

Figure 4.1: LDV scheme used to carry out the modal test [10].

Another crucial concern, particularly in modal analysis, is the alignment of the laser beam concerning velocity components. When the object under study predominantly exhibits out-of-plane velocity components, aligning the laser beam is more manageable (what will be the case with this work). Additionally, implementing this equipment can be challenging in structures that limit light diffusion, such as those in aerospace applications, and in environments with high dust levels. The presence of dust particles can significantly impact the air's refractive index, potentially leading to notable experimental errors.

5. Experimental Procedures

5.1. Configuration of points to be measured

As mentioned earlier, the experimental focus is on studying all modal shapes up to the 5^{th} flexural mode. Therefore, when configuring measurement points, it's important to aid the LDV software in accurately representing these modal shapes.

In numerical analyses, it was observed that both flexural and torsional modal shapes exhibit a parabolic pattern along the x-axis. Consequently, selecting only the maximum and minimum points, known as nodes where the modal shape remains still, might lead to a representation of linear motion, failing to capture the parabolic nature of these modes. Thus, given the time limitations of the laboratory activity and the fact that more points would require additional laser time, the choice of measurement points needed to strike a balance between quality and time optimization for the task at hand.

The chosen point configuration, depicted in Figure 5.1, primarily focused on the 5^{th} flexural mode, which is more complex. This strategy involved placing points on the symmetry of the *y-axis* where maximum displacements were expected and near areas likely to exhibit maximum displacements for that specific modal shape. The aim was to aid the software in accurately representing the parabolic behaviour observed in the numerical modes. This approach effectively represented all flexural modal shapes, because some of the 23 selected points also served as minimum and maximum points for earlier flexural modes and using 23 points were deemed sufficient for accurately representing lower-order flex-

ural modal shapes.

It's worth noting that the chosen point configuration wouldn't allow for the determination of torsional frequencies and their corresponding modal shapes. This limitation arises from the fact that these points are positioned on the $y - axis$ of symmetry, which serves as a nodal line for all torsional modal shapes. To address this, the same line of points was duplicated 30 cm above and 30 cm below, based on numerical results suggesting that these lines should no longer act as nodal lines for torsional modal shapes.

Furthermore, the point configuration presented in Figure 5.1 was consistently used for all the beams under study. This uniformity is maintained despite variations in modal form frequencies and sequences across different beams. Even when torsional modes precede flexural modes, the positions of all nodal lines remain consistent across all modal forms for all beams.

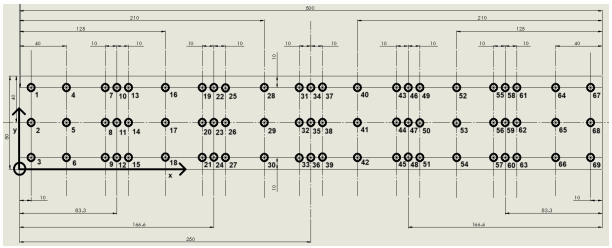

Figure 5.1: Point configuration chosen to take measurements.

5.2. **Procedures carried out on the beams**

After configuring the measurement points, a preliminary test was conducted to check the ability of the aluminium surface to effectively reflect laser light. This concern arose due to the known issue that aeronautical surfaces often have limited light reflectivity. The test confirmed that these sandwich beams faced the same challenge, and it was evident that without addressing this issue, reliable results could not be obtained. To overcome this problem, small pieces of reflective tape were applied only at the measurement points, allowing the LDV to capture the beam's signal effectively and ensuring the experiment's reliability.

5.3. **Structure assembly**

The structure used for this experimental activity was a square metal frame with circular through holes and the structure was secured to a dedicated table through these holes using screws and nuts (as depicted in Figure 5.2).

To connect the beams under study to this metal frame, various methods were tested. Since the aim was to study the beams in a **Free-free condition**, the goal was to introduce as little rigidity as possible into the system. None of the configurations allowed for movement along the y-axis. Consequently, due to the inability to achieve a truly Free-free condition for the beams, the study of flexural modal shapes in that plane had to be disregarded. Thus, the focus was on selecting a configuration that minimized stiffness in the directions where the beams could move. As a result, the configuration with the least introduced rigidity in the systems is shown in Figure 5.2.

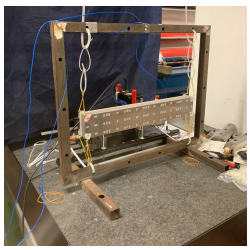

Figure 5.2: Configurations useded for carrying out the experimental activity.

5.4. **Shaker assembly**

The process of connecting the Shaker to the same table where the rest of the structure was located involved using screws and nuts. Next, the tip of the Shaker arm was affixed to the beam. This attachment point was positioned at approximately 350 cm from the *x-axis* origin and 25 cm from the *y-axis* origin. Special care was taken to prevent any bending of the Shaker arm, because avoiding this bending effect, ensured that this connection wouldn't create an additional point of support, minimizing any extra stiffness it might introduce to the structure.

5.5. **Laser assembly**

Initially, a dark cloth was positioned behind the entire structure under study to minimize ambient light interference. Subsequently, the user support document for the device was consulted to identify the best distance for laser placement [11]. The document revealed that there were several optimal distances for maximizing the LDVs ability to capture the laser light effectively. Given the laboratory's space limitations, it was decided to position the LDV at 1365 mm, which corresponds to the 7^{th} optimal distance.

6. Results

6.1. **Previous considerations**

Before delving into the analysis of the results, it's crucial to highlight several key aspects to ensure a comprehensive understanding of the obtained outcomes.

Firstly, due to structural constraints during the assembly, the Shaker had to be positioned 350 cm from the x-axis origin and 25 cm from the y-axis origin. However, a detailed analysis of the numerical models suggested that this specific location is close to a node for the 4^{th} flexural modal shape. This means that, according to Equation 2.16, $\hat{\phi}_{k\beta}$ will be close to zero for this mode since this point serves as

a node for the 4^{th} flexural mode. Consequently, the frequency peak for this mode is expected to be less prominent, rendering it less evident in the results.

In addition, in our results analysis, numerical transfer functions will be compared with specific experimental data from Point 1, as illustrated in Figure 5.1. This point was selected because it is expected not to correspond to a node for any of the studied modal shapes, enabling us to observe all the associated frequency peaks.

To create numerical FRF graphs for these points, an intermediate process was necessary because Patran/Nastran doesn't directly provide this data. Initially, modal vectors relating to these points' displacements were extracted from Patran, and a MATLAB script was developed to process and extract these values. For a meaningful comparison, both numerical and experimental transfer functions were normalized by dividing them by their respective maximum values. Also, it's worth noting that the constants, represented as ζ_k in Equation 2.16, were estimated following the procedure outlined in Chapter 2.3

Finally, to compare the differences between the frequencies obtained for the modal shapes in numerical and experimental models (dif), Equation 6.1 was utilized. Here, f_{FE} denotes the frequencies from the numerical model, and f_{Exp} denotes the frequencies from the experimental model.

$$dif = \frac{f_{FE} - f_{Exp}}{f_{FE}} \times 100 \qquad (6.1)$$

This difference was calculated in that way because the simulation of the Free-free condition can only be done numerically.

6.2. Evaluation of the quality of results

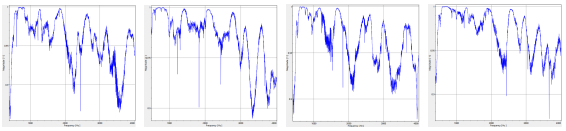

(a) Graph obtained for coherence for beam D01. (b) Graph obtained for coherence for beam D02. (c) Graph obtained for coherence for beam D03. (d) Graph obtained for coherence for beam D04.

Figure 6.1: Graphs obtained for the average coherence of all the experimental tests that will be analysed.

From the analysis of the graphs in Figure 6.1, it's evident that the coherence values for all experimental tests were very high, close to 1. While minor oscillations were observed, particularly at the resonant frequencies, the coherence function consistently remained close to 1, with minimum values never falling below 0.85. This indicates that noise had a negligible impact on the results obtained. Consequently, the analyses that will be performed next should be a fair representation of the reality under study.

6.3. Analysis of the D01 beam

numerical modal forms		experimental modal forms			differences (%)
modal shape type	frequency Hz	modal shape type	frequency Hz	ζ (%)	
1^{st} torsional	704.97	1^{st} flexu-torsional	767.5	0.68	6.81
1^{st} flexural	715.22				
2^{nd} flexural	1169.4	2^{nd} flexural	1280	1.71	9.46
2^{nd} torsional	1602.4				
3^{rd} flexural	1669.8	3^{rd} flexural	1862.5	1.68	11.54
4^{th} flexural	2101.5	4^{th} flexural	2377.5	1.81	13.12
3^{rd} torsional	2538.1	3^{rd} torsional	2768.75	1.81	9.09
5^{th} flexural	2589.2	5^{th} flexural	2880	2.19	11.23

Table 6.1: Results obtained for the modal forms of beam D01.

After examining Table 6.1, it's clear that the experimental modal shapes, despite not including the second torsional mode, follow the same order as the numerical ones. Notably, the differences between the models, while significant, consistently fall within a range of 6.81% to 13.12%.

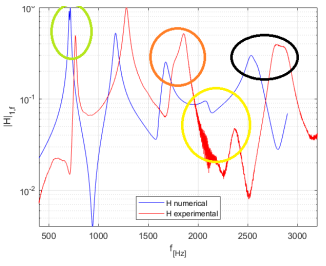

Figure 6.2: Experimental FRF for point 1 of beam D01.

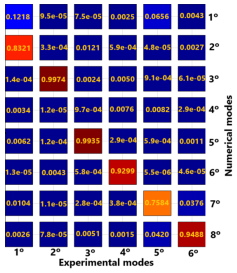

Figure 6.3: MAC analysis results for beam D01.

Furthermore, by observing Figure 6.2 it is possible to see that the numerical and experimental FRF graphs show a consistent pattern. Numerical data exhibit earlier frequency peaks than the experimental data, as expected. The 4^{th} flexural modal shape lacks distinguishing features in both sets of data (yellow circle). Furthermore, the presence of a plateau in both sets of FRFs for the 3^{rd} torsional and 5^{th} flexural modal shapes (black circle) likely accounts for the observed frequency differences in Table 6.1. Regarding the 1^{st} flexural and 1^{st} torsional modal shapes, while the numerical FRF displays two closely spaced yet distinct frequency peaks, the experimental FRF does not, leading to the identification of a 1^{st} flexo-torsional modal shape (green circle). Additionally, a single narrow peak characterizes the 2^{nd} torsional and the 3^{rd} flexural modes (orange circle), indicating that these modes might be too close together for clear differentiation, particularly when considering the values of ζ.

The MAC analysis, presented in Figure 6.3, delivered generally positive results. Except for the

1^{st} and 5^{th} experimental modes, all other modes displayed strong correlations (above 0.92) with individual numerical modes. This supports the prior statement that the first experimental mode corresponds to a 1^{st} flexo-torsional mode. This is evident from the mode's resemblance to the 1^{st} torsional numerical mode by approximately 12% and the 1st flexural numerical mode by about 82%. It's worth emphasizing that, despite the 4^{th} and 5^{th} experimental modes showing substantial correlations with their respective numerical modes, these correlations were slightly weaker (0.92 and 0.73, respectively)

6.4. **Analysis of the D02 beam**

numerical modal forms		**experimental modal forms**			**differences** (%)
modal shape type	frequency Hz	modal shape type	frequency Hz	ζ (%)	
1^{st} flexural	753.14	1^{st} flexural	795	1.15	5.56
1^{st} torsional	846.32	1^{st} torsional	920	1.56	8.71
2^{nd} flexural	1344.4	2^{nd} flexural	1436.25	1.66	6.83
2^{nd} torsional	1798.5	2^{nd} torsional	1940	2.53	7.87
3^{rd} flexural	1947.3	3^{rd} flexural	2125	1.84	9.13
4^{th} flexural	2489.8	4^{th} flexural	2773.75	1.94	11.40
3^{rd} torsional	2795.3	3^{rd} torsional	3018.75	2.90	7.99
5^{th} flexural	3055.9	5^{th} flexural	3320	1.92	8.64

Table 6.2: Results obtained for the modal forms of beam D02.

Table 6.2 clearly illustrates that the order of experimental modal shapes from this beam aligns with that of the numerical modal shapes. The frequency differences between the numerical and experimental models are notably significant for this beam, ranging around 5.56% but never exceeding 11.40%.

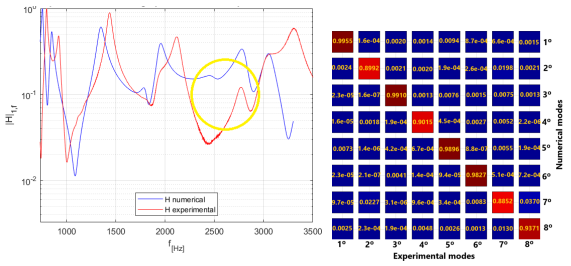

Figure 6.4: Experimental FRF for point 1 of beam D02.

Figure 6.5: MAC analysis results for beam D02.

An inspection of Figure 6.4 reveals that point 1 doesn't correspond to any node for the examined modal shapes, as anticipated. Furthermore, it's essential to recognize that, similarly to previous observations, both the numerical and experimental FRFs share a consistent trend. Additionally, the 4^{th} flexural mode's lack of significance, both in numerical and experimental contexts (highlighted by the yellow circle), may contribute to the larger observed frequency difference for this mode (Table 6.2).

From the analysis of Figure 6.5, it can be observed that satisfactory results were obtained in the MAC analysis for this beam. This is evident from the high degree of similarity among all diagonal elements in the matrix. Notably, only the 2^{nd}, 4^{th}, and 7^{th} modes in both models exhibited a slightly lower level of resemblance among themselves, never falling below 88%. Another noteworthy observation is that each mode in each model closely corresponds to one mode in the other model. This once again underscores that the numerical model can be a good approximation of the studied reality.

6.5. **Analysis of the D03 beam**

numerical modal forms		**experimental modal forms**			**differences** (%)
modal shape type	frequency Hz	modal shape type	frequency Hz	ζ (%)	
1^{st} flexural	620.64	1^{st} flexural	662.5	0.84	6.74
1^{st} torsional	693.14	1^{st} torsional	770	1.68	11.09
2^{nd} flexural	1052.6	2^{nd} flexural	1158.75	1.57	10.08
2^{nd} torsional	1508.7				
3^{rd} flexural	1511.8	3^{rd} flexural	1690	2.08	11.79
4^{th} flexural	1925.3	4^{th} flexural	2210	1.54	14.78
3^{rd} torsional	2310.5				
5^{th} flexural	2373.5	5^{th} flexural	2660	1.87	12.07

Table 6.3: Results obtained for the modal forms of beam D03.

From Table 6.3, it's evident that the experimental modal shapes align with the numerical modal shapes' order, despite the inability to identify the 2^{nd} and 3^{rd} torsional modes. Notably, substantial differences between the two models, ranging from 6.74% to 14.78%, are observed, particularly for the higher-order modal shapes. This disparity may stem from the close proximity of these higher-order modal shapes to others that the LDV couldn't identify.

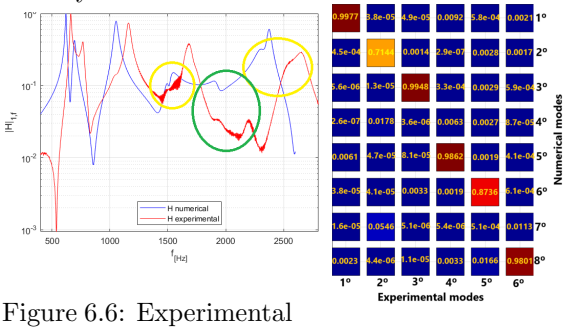

Figure 6.6: Experimental FRF for point 1 of beam D03.

Figure 6.7: MAC analysis results for beam D03.

An analysis of Figure 6.6 reveals several significant findings. Firstly, point 1 is evidently not associated with a node for any of the studied modal shapes, as indicated by the presence of frequency peaks in earlier graphs. Both the numerical and experimental FRFs display a similar trend. Notably, the previously plotted frequency peaks, which the

LDV struggled to identify, are challenging to observe for both models. This suggests that since these peaks were very close together numerically before accounting for damping values, considering them made it impossible to clearly distinguish them in the numerical FRF, which also justifies their absence in the experimental FRF. This may support the hypothesis that it was rather difficult for the LDV to identify these supposed modal shapes (indicated by the yellow circles). Furthermore, the 4^{th} torsional modal shape remains less distinct for this beam, potentially accounting for the greater frequency differences observed between models for this mode, as shown by the green circle.

Analyzing Figure 6.7, it's clear that except for the 2^{nd} and 5^{th} experimental modes, all other experimental modes exhibit a very high degree of similarity with a single numerical mode, with MAC values consistently above 0.98. It's also worth noting that neither the 4^{th} nor the 7^{th} numerical modes correlate with any of the experimental modes, which supports the previously proposed hypothesis that the LDV was unable to identify two potential frequency peaks that would likely correspond to these numerical modes.

6.6. **Analysis of the D04 beam**

numerical modal forms		**experimental modal forms**			**differences** (%)
modal shape type	frequency Hz	modal shape type	frequency Hz	ζ (%)	
1^{st} flexural	647.61	1^{st} flexural	653.75	1.52	0.95
1^{st} torsional	827.48	1^{st} torsional	880	2.35	6.35
2^{nd} flexural	1208.3	2^{nd} flexural	1286.75	1.42	6.49
2^{nd} torsional	1712.7				
3^{rd} flexural	1770.5	3^{rd} flexural	1940	1.79	9.57
4^{th} flexural	2289.5	4^{th} flexural	2575	1.97	12.47
3^{rd} torsional	2583.7	3^{rd} torsional	2827.5	2.75	9.44
5^{th} flexural	2815.7	5^{th} flexural	3098.75	1.98	10.05

Table 6.4: Results obtained for the modal forms of beam D04.

Upon reviewing the Table 6.4, it's clear that the experimental modal shapes follow the same order as the numerical modal shapes, despite the 2^{nd} torsional mode not being identified. Notably, there are significant differences between the models, especially for modal shapes above 1700 Hz, where the discrepancies range from 9.57% to 12.47%. However, these differences were lower for this specific beam compared to the other beams studied. It's essential to emphasize that the 4^{th} flexural mode exhibited the highest difference of frequency, which further supports the earlier hypothesis that the Shaker's positioning might have negatively influenced the visualization of this modal shape.

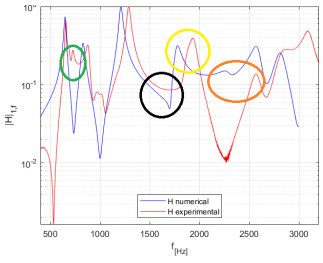

Figure 6.8: Experimental FRF for point 1 of beam D04.

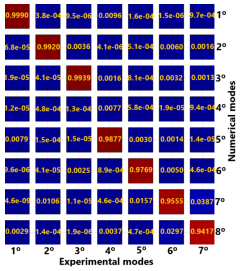

Figure 6.9: MAC analysis results for beam D04.

Upon analyzing Figure 6.8, several key observations become apparent. Firstly, it's clear that point 1 doesn't correspond to a node for any of the analyzed modal shapes, as all the related frequency peaks were observed in the previous plots. Furthermore, it's noteworthy that the numerical and experimental FRF plots exhibit some degree of similarity, with the frequency peaks of the numerical model appearing before those of the experimental model. Another important finding is the absence of a frequency peak corresponding to the 2^{nd} torsional mode in both the experimental and numerical FRF plots (indicated by the black circle). Moreover, the peak related to the 3^{rd} flexural mode appears slightly broader in both models, suggesting that the 2^{nd} torsional mode may have mixed with this modal shape (indicated by the yellow circle). Additionally, it's confirmed that the frequency peak detected by the laser at 722.5 Hz is exclusive to the experimental model (indicated by the green circle). However, it's uncertain if this peak corresponds to a specific modal shape since there is no significant phase change. Lastly, it's evident that the peak associated with the 4^{th} flexural mode lacks significance (orange circle), further supporting the idea that the greater frequency difference observed for this modal shape is attributable to the Shaker's positioning.

The analysis of Figure 6.9 reveals that each experimental mode closely corresponds to the corresponding numerical mode, with consistently high similarity values observed in all cases (the lowest value observed was approximately 0.94 for the relationship between the 7^{th} experimental mode and the 8^{th} numerical mode). Additionally, it can be inferred that the 4^{th} numerical mode did not correlate with any other experimental mode, indicating that this mode might have mixed with the 3^{rd} flexural mode. It's also worth noting that the MAC analysis values for this beam were higher than those obtained for any of the other beams studied.

6.7. **Hammer Test**

The observed discrepancies between the numerical and experimental models for all beams studied were around 10%. This raised a hypothesis that the

Shaker introduced significant stiffness at the contact point with the structure, potentially altering the natural frequencies of the experimental model. To explore this, the Shaker was disconnected from beam D02, and the structure was excited using an Impact Hammer.

Shaker Test		**Hammer Test**	
frequencies [Hz]	diferences with numerical model (%)	frequencies [Hz]	diferences with numerical model (%)
795	5.56	788.75	4.51
920	7.44	923.75	7.87
1436.25	6.83	1452.5	8.04

Table 6.5: Comparison of the results obtained for all the experiments for beam D02.

Upon examining Table 6.5, it's evident that the results from the experimental tests using the Shaker and the Impact Hammer show relatively minor differences. Specifically, only the first natural frequency obtained with the Impact Hammer is slightly lower than that obtained in the Shaker test (by approximately 7 Hz). This suggests that the investigated issue is not significant and is unlikely to be the primary cause of the notable disparities between the numerical and experimental models.

7. Conclusions

First and foremost, the use of the LDV proves to be a favourable alternative for conducting this type of experimental work, as evident from consistently very high values for the coherence function (always above 0.85).

Furthermore, it's notable that the frequencies of the experimental modal shapes consistently exceeded those of the numerical modal shapes, with differences typically around 10% (slightly greater for higher-frequency modal shapes). Despite these distinctions, the shared modal order and the observed coherence in the FRF plots for both models, which exhibited a similar trend, lead to the conclusion that the numerical models can be considered a robust approximation of the studied reality. This conclusion finds additional support in the MAC analyses, where, with few exceptions involving insignificant frequency differences between modal shapes, all modal shapes had values above 0.95.

Additionally, based on the results presented before, it can be concluded that beams D02 and D04 were the most suitable for experimental analysis. For the first beam, all experimental modal shapes were obtained, while for D04, only the 2^{nd} torsional mode was not acquired. Also, it's crucial to note that the 4^{th} flexural mode consistently exhibited the highest differences in all beams. This strengthens the earlier hypothesis that the Shaker's placement might impede the acquisition and visualization of this specific modal shape.

Finally, regarding the Shaker's influence, it was determined that it doesn't significantly affect the structures under examination. Nevertheless, one potential contributor to stiffness, which cannot be dismissed, is the configuration itself used to simulate the Free-free condition.

References

[1] Y. G. Z. Ru-Min Wang, Shui-Rong Zheng, *Polymer Matrix Composites and Technology*, 1st ed. Woodhead Publishing, jul 2011.

[2] V. V. Vasiliev and E. V. Morozov, *Advanced Mechanics of Composite Materials and Structural Elements*, 4th ed. Elsevier, jun 2018.

[3] J.-C. Chen, "Evaluation of modal testing methods," in *25th Structures, Structural Dynamics and Materials Conference*, 1984.

[4] M. Peeters, G. Kerschen, and J.-C. Golinval, "Modal testing of nonlinear vibrating structures based on nonlinear normal modes: Experimental demonstration," *Mechanical Systems and Signal Processing*, vol. 25, no. 4, pp. 1227–1247, 2011.

[5] P. M. Gherlone, "Lezioni di dinamica delle strutture aerospaziali," 2023, [Slides from the course Dynamics of structures of the aerospace engineering course at PoliTO].

[6] M. F. Green, "Modal test methods for bridges: a review," in *Proceedings-Spie the International Society for Optical Engineering*. Citeseer, 1995, pp. 552–552.

[7] F. Falcetelli, A. Martini, R. Di Sante, and M. Troncossi, "Strain modal testing with fiber bragg gratings for automotive applications," *Sensors*, vol. 22, no. 3, 2022. [Online]. Available: https://www.mdpi.com/1424-8220/22/3/946

[8] Z. Ibrahim and P. Reynolds, "Modal testing of a cantilever grandstand," in *Proceedings of the International Conference on Construction and Building Technology (ICCBT'08)*, 2008.

[9] P. Castellini, M. Martarelli, and E. Tomasini, "Laser doppler vibrometry: Development of advanced solutions answering to technology's needs," *Mechanical Systems and Signal Processing*, vol. 20, no. 6, pp. 1265–1285, 2006, special Issue: Laser Doppler Vibrometry. [Online]. Available: https://www.sciencedirect.com/science/article/pii/S0888327005002220

[10] P. C. e. Enrico Primo Tomasini (editor), *Laser Doppler Vibrometry: A Multimedia Guide to its Features and Usage*, 1st ed. Springer, 2020.

[11] Polytec, *Operating Instructions Polytec Scanning Vibrometer, PSV-500-3D.*